Influence of Ni^{2+} ions on the structural, morphological, photoluminescence, photo-catalytic and anti-bacterial studies of Cd$_{0.9}$Zn$_{0.1}$S nanostructures

P. Raju[1,4,*] , Joseph Prince Jesuraj[2], and S. Muthukumaran[3]

[1] *Department of Physics, H.H. The Rajah's College, Pudukkottai, Tamilnadu 622 001, India*

[2] *Department of Physics, Bharathidasan Institute of Technology Campus, University College of Engineering, Anna University, Tiruchirappalli, Tamilnadu 620 024, India*

[3] *Department of Physics, , Government Arts College, Melur, Madurai, Tamilnadu 625106, India*

[4] *Manonmaniam Sundaranar University, Abishekapatti, Tirunelveli, Tamilnadu 627 012, India*

ABSTRACT

The present investigation reported the controlled synthesis of Cd$_{0.9}$Zn$_{0.1}$S and Cd$_{0.89}$Zn$_{0.1}$Ni$_{0.01}$S nanostructures by simple chemical co-precipitation route. The XRD analysis confirmed the cubic structure of CdS on Zn doped CdS and Zn, Ni dual doped CdS without any secondary/impurity phases and no alteration in CdS cubic phase was noticed by Zn/Ni addition. The shrinkage of crystallite size from 69 to 43 Å and the variation in lattice constants and micro-strain were described by the addition of Ni and the defects associated with Ni^{2+} ions. Microstructural and optical studies of the prepared films were carried out using scanning electron microscope (SEM), UV-visible spectrometer and photolumi-nescence (PL) spectra. The enhanced optical absorbance in the visible wavelength and the reduced energy gap by Ni substitution showed that Cd$_{0.89}$Zn$_{0.1}$Ni$_{0.01}$S nanostructures are useful to improve the efficiency of opto-electronic devices. The functional groups of Cd-S/Zn-Cd-S/Zn/Ni-Cd-S and their chemical bonding were verified by Fourier transform infrared (FTIR) studies. The elevated visible PL emissions such as blue and green emissions by Ni addition was explained by decreasing of crystallite size and generation of more defects. Zn, Ni dual doped CdS nanostructures are identified as the probable an efficient photo-catalyst for the degradation of methylene blue dye. The liberation of more charge carriers, better visible absorbance, improved surface to volume ratio and the creation of more defects are accountable for the current photo-catalytic activity in Zn/Ni doped CdS which exhibited better photo-catalytic stability after sex cycling process. The better bacterial killing ability is noticed in Ni doped Cd$_{0.9}$Zn$_{0.1}$S nanostructure which is due to the collective effect of lower particle/grain size and also higher ROS producing capacity.

Address correspondence to E-mail: praju12345@yahoo.com

1 Introduction

ZnS, ZnO, CdS and CdO semiconducting materials in the form of nano-scale are focused significant consideration in the emitting devices such as light emitting diodes (LEDs) owing to their modified band gap [1, 2]. CdS is one of the significant and useful materials with band gap $\sim$ 2.42 eV [3] and hence it is effectively applied in electroluminescent devices [4], optoelectronic devices [5], photoluminescent [6, 7], photo-detectors, window glass coating [8], and transistors and LEDs [9]. Wide band gap CdS nanoclusters are often employed as barricades to the solar radiation in 515 nm [10]. CdS exhibits different structures such as wurtzite, hexagonal and rock salt [11] where hexagonal structure is thermodynamically steady at room temperature conditions and cubic structure exist under very small sized particles [4]. CdS may be changed over to hexagonal structure from cubic structure by creating defects and stacking faults within the semiconducting materials [12].

The CdS semiconductors doped with impurity element like Zn and Ni achieved the wide-ranging technological as well as the scientific application in nano-electronics [13], and the nanomaterials added with magnetic elements are of interest for their important applications in spin based electronic instruments [14]. The effect of transition metal (TM) ions doped into CdS material has showed an enormous attraction as it modifies its optical, structural and luminescence properties [15, 16] and applied for different potential applications [17]. The addition of TM ions such as Zn, Fe, Cu, Ni, Mn, etc. into CdS enhanced the electrical, optical and photoluminescence properties [18] and also the formation of new materials with innovative properties are expected [19]. In the existing work, Zn is preferred as the first doping element into CdS. Zn is one among the significant TM elements having an ionic radius of 0.074 nm which is smaller than that of Cd^{2+} which has the ionic radius of 0.097 nm. Therefore, Zn^{2+} can easily enter inside the Cd-S lattice and modify its structural, optical and physical properties by restoring the Cd^{2+} ions [20].

Moreover, the incorporation of Zn enhances the band gap of the CdS nanostructure without changing its basic lattice structure [21]. The addition of Zn improves the photo-catalytic performance of CdS by increasing the photo-catalysis stability and surface to volume ratio of the material [22] which is highly essential to develop an innovative materials. Based on the comprehensive investigation of morphology, structure and photoluminescence properties of Zn doped CdS nanostructures from the previous literature [23], Zn doping level is optimized as 10% ($Cd_{0.9}Zn_{0.1}S$).

Generally, the addition of second dopant is useful to enhance its physical and chemical properties of Zn doped CdS [24]. In order to enhance the structure, optical and photoluminescence behaviour of $Cd_{0.9}Zn_{0.1}S$ nanostructures without creating additional impurity/secondary phases, Ni is selected as one more doping element into Zn-doped CdS. The addition of Ni considerably enhances the absorption and transmittance properties of CdS and shift the optical absorption and other responses towards the higher wavelength region i.e., visible wavelength ranges which is useful to improve the photo-catalytic behaviour under sun light radiation [25]. Taheri et al. [26] reported that the replacement of Ni^{2+} ions produces the extra deep energy levels closer to the conduction band of CdS and they acted as efficient luminescence activation centres. The size reduction and enhancement in band gap by Ni addition through Cd-S lattice makes them as front lining materials in light emitting devices, solar cells and photo-catalytic applications [27]. The lower ionic radius of Ni^{2+} ions (0.069 nm) than Cd^{2+} ions and the higher electro-negativity (1.91 Pauling) of Ni^{2+} than Cd^{2+} ions which has electro-negativity of $\sim$ 1.61 Pauling [28] improves the conducting properties of Ni added CdS nanostructures.

It is noticed from the literature that the addition of Ni and Fe plays as a quenching centers for photo as well as fluorescence conduction and they reported that the decrease of quantum size yields in the higher wavelength region and the consequences in smaller carrier lifetimes helpful in advanced opto-electronic applications [29, 30]. Singh et al. [31] reported that Ag^{+} and Cu^{2+} doping of CdS enhanced the optical, distortion in crystal structure, and better photocatalytic properties and they described that the addition of Ag^{+} and Cu^{2+} in CdS induced the narrowing of band edge potentials and distortion in the crystal. Aimouch et al. [32] discussed that the energy gaps of Mn-doped as well as Mn, Cr dual doped materials are superior than pure CdS which generating the more interesting for probable technological applications for high density magneto-optical recording.

Even though, the systematic and complete studies on morphology, structure and optical investigations

of Zn or Ni doped CdS nanostructures were made [20–28], the comprehensive analysis of Zn and Ni dual doped CdS nanostructures is nearly scanty. Hence, the present work focused on the successful preparation of $Cd_{0.9}Zn_{0.1}S$ and Ni = 1% doped $Cd_{0.9}Zn_{0.1}S$ with the help of co-precipitation route. Since, the addition of Zn and Ni induced the modification in structural and optical properties, the detailed morphological, structural, optical, photoluminescence, photo-catalytic and anti-bacterial investigations have been made on Zn-doped CdS and Zn, Ni dual doped CdS nanostructures and the acquired outcomes are interpreted.

2 Experimental details

2.1 Synthesis of Ni-doped Cd0.9Zn0.1S (Ni = 0 and 1) nanostructures

Zn and Ni dual substituted CdS nanostructures were prepared with the help of co-precipitation method. The co-precipitation route is preferred in this work due to its different advantages such as possibility to change the wide range of impurity concentrations, better quality of the samples and controlled doping [33].

Cadmium acetate dihydrate ($Cd(CH_3COOH)_2·2H_2O$), Nickel acetate tetrahydrate ($Ni(CH_3-COO)_2·4H_2O$), zinc acetate dihydrate [$Zn(CH_3COO)_2·2H_2O$], and sodium sulfide (Na_2S) have been used as the precursors for the preparation of Zn and Ni dual doped CdS without additional purification. The entire chemical engaged in this work were analytical grade (AR) and high purity (> 99% purity). The chemicals, $Cd(CH_3COOH)_2·2H_2O$, $Ni(CH_3COO)_2·4H_2O$, $Zn(CH_3COO)_2·2H_2O$, and Na_2S were procured from M/s. Merck chemical company and they are the source of Cd^{2+}, Zn^{2+}, Ni^{2+} and S^{2-} ions, respectively. The procedure to the prepare the above material is as reported in the our previous paper [23]. The flowchart and the procedures for the preparation of Zn and Ni dual doped CdS nanostructures is as shown in Fig. 1.

To synthesis dual doped CdS nanostructures with Zn and Ni, separate solutions were prepared by dissolving 0.89 M cadmium acetate, 0.1 M zinc acetate, 1 M sodium sulfde, 0.01 M chromium chloride in 50 ml double distilled water. These solutions were stirred individually with a magnetic stirrer until the chemicals were completely dissolved. All solutions were allowed to mix drop wise in a common beaker, which is kept on continuous stirring at a rate of 1000 rpm for 8 h. The pH value of the solution was maintained at 9 by adding appropriate aqueous ammonia solution. After the reaction was completed, a precipitate was deposited at the bottom of the flask. In order to eliminate any unwanted impurities the obtained nearly yellow colour output was filtered out, washed many times with high purity de-ionized water and methanol. The collected wet precipitates were dried using a furnace at 90 °C for 10 h to eliminate moisture content.
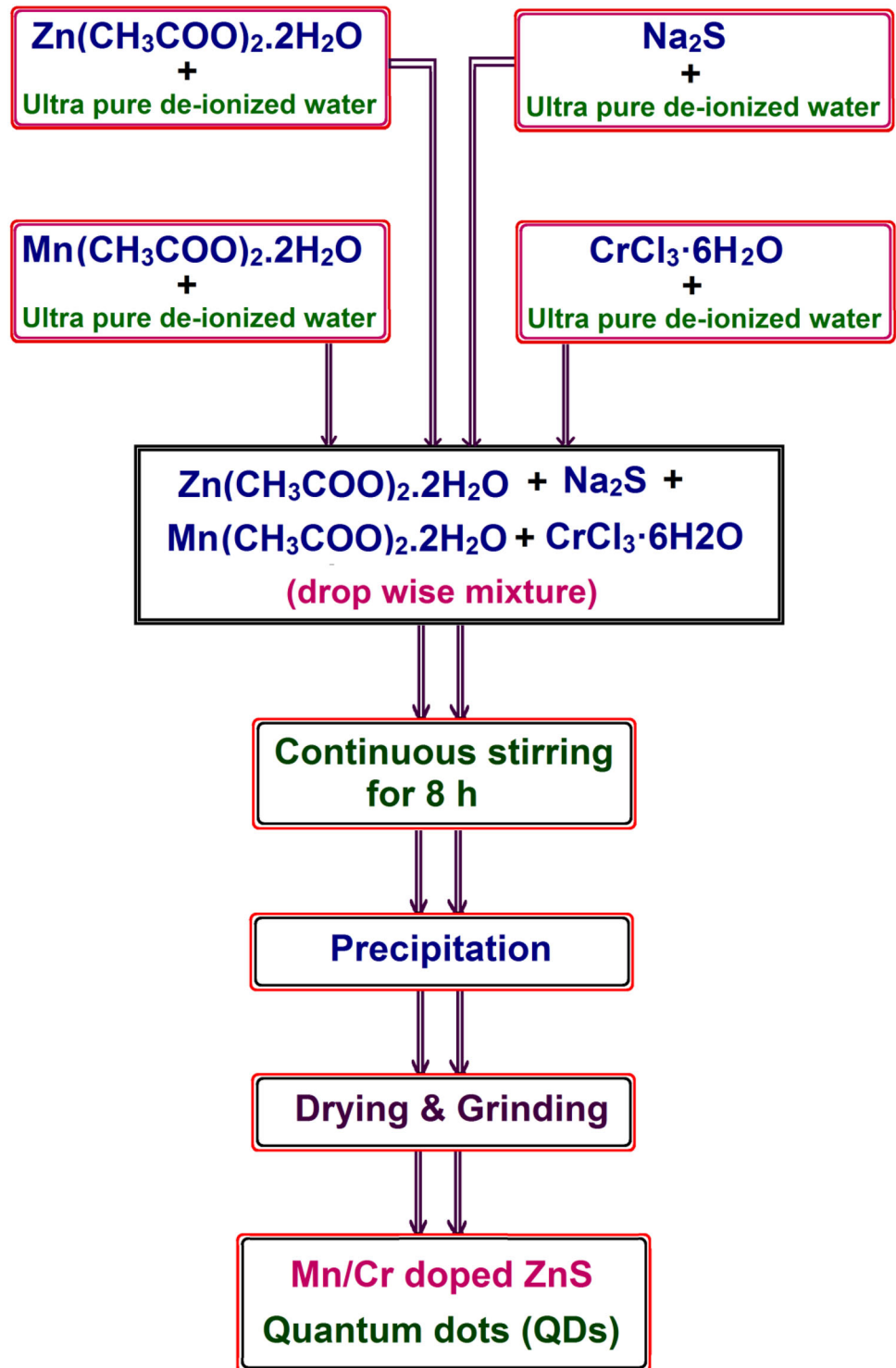
The chemicals used to synthesize $Cd_{0.9}Zn_{0.1}S$ and $Cd_{0.89}Zn_{0.1}Ni_{0.01}S$ nanostructures with their chemical formulae are presented in Table 1. The color of the attained nanostructure of $Cd_{0.9}Zn_{0.1}S$ is found to be yellow that is altered to brown for Ni = 1% doped $Cd_{0.9}Zn_{0.1}S$ as shown in Fig. 2.

2.2 Characterization techniques

The structure of the synthesized materials is obtained by X-ray diffraction (XRD) technique [34–37]. The diffracted patterns of the synthesized samples have been carried out using RigaKuC/max-2500 diffractometer with Cu Kα radiation from $2\theta = 20°$ to $60°$ with a scan rate of $0.04°/S$. The microstructure was also examined by transmission electron microscopy (TEM, Philips- CM200) in the range of operating voltage as 20–200 kV. The presence of constitutional elements like Cd, Ni, Zn and S were confirmed by energy dispersive X-ray spectrometer on K and L lines. The optical absorption spectra have been obtained using UV–Visible spectrometer (Model: lambda 35, Make: Perkin Elmer) from 300 to 550 nm at ambient temperature with necessary software. The presence of chemical bonding was studied by FTIR spectrometer (Model: Perkin Elmer, Make: Spectrum RX I) from 400 to 4000 cm^{-1}. The photoluminescence (PL) spectra were carried out between the wavelength from 350 to 640 nm using a fluorescence spectrophotometer (F-2500, Hitachi) at room temperature. Here, the excitation wavelength is chosen as 320 nm which is nearly equal to the energy gap of the prepared material.

Photocatalytic activities of the synthesized samples were carried out on methylene blue (MB) using UV–vis spectrophotometer. MB stock solution (2 mmol) was prepared in de-ionized (DI) water. 50 ml of

Fig. 1 Flowchart and the preparation steps for the preparation of Zn and Ni dual doped CdS nanostructures using chemical precipitation method

prepared MB solution (reactant) was taken into a 100 ml beaker and kept on the magnetic stirrer. Subsequently, 10 mg of the catalyst (synthesized samples) was added into the reactant and irradiations were carried out under UV light (wavelength 360 nm, distance 80 mm, power 80 W) under mild stirring. After UV irradiation, 1 ml of the solution was taken out from the solution at certain time intervals (0 to 3 h) and centrifuged to get the upper clear solution.

Table 1 Chemicals used to synthesize $Cd_{0.9}Zn_{0.1}O$ and $Cd_{0.89}Zn_{0.1}Ni_{0.01}O$ nanostructures with their chemical formulae

Samples	Chemicals	Chemical formulae
$Cd_{0.9}Zn_{0.1}S$	Cadmium acetate dihydrate	$Cd(CH_3COOH)_2 \cdot 2H_2O$
	Zinc acetate dihydrate	$Zn(CH_3CO_2)_2 \cdot 2H_2O$
	Sodium sulfide	Na_2S
$Cd_{0.89}Zn_{0.1}Ni_{0.01}S$	Cadmium acetate dihydrate	$Cd(CH_3COOH)_2 \cdot 2H_2O$
	Zinc acetate dihydrate	$Zn(CH_3CO_2)_2 \cdot 2H_2O \ Ni(CH_3COO)_2 \cdot 4H_2O$
	Nickel acetate tetrahydrate	Na_2S
	Sodium sulfide	

Antibacterial activity of the prepared nanoparticle was determined using well diffusion method using Mueller Hinton agar media. Mueller Hinton agar media was purchased from Millipore Sigma (catalog no. 70191). After sterilization and solidification process, wells were cut on the Mueller Hinton agar using cork borer. Two bacteria *Staphylococcus aureus* (gram positive derived from ATCC 25923) and *Escherichia coli* (gram negative derived from ATCC 23724) were taken for the study. These bacterial pathogens were swabbed onto the surface of Mueller Hinton agar plates. Wells were impregnated with the test samples of concentration 50 mg/l with norfloxin 10 μg as the standard. The plates were incubated for 30 min to allow the extract to diffuse into the medium. The plates were incubated at 37 °C for 24 h, and then the zone of inhibition was measured in millimeters. Each antibacterial assay was performed in triplicate and mean values were reported.

3 Result and discussions

3.1 X-ray diffraction (XRD) – structural studies

The XRD spectra is one of the potent tools to investigate and analyze the structure, size and strain of the materials. The XRD patterns of $Cd_{0.9}Zn_{0.1}S$ and $Cd_{0.89}Zn_{0.1}Ni_{0.01}S$ nanostructures between 20 and 60° are presented in Fig. 3. The observed wide diffraction peaks from Fig. 3 indicate that the prepared system contains particles/grains existing in the nano-lelvel crystalline nature. Even though three major orientations have been noticed along (111), (220) and (311) orientations, (111) orientation is chosen for size and micro-strain assessment due to its dominant intensity. The diffraction peaks found in $Cd_{0.9}Zn_{0.1}S$ nanostructure are well-suited with the cubic phase of CdS (JCPDS card no.: 10-454) [38]. The addition of Ni

stimulates some fraction of hexagonal phase in the Cd-Zn-S lattice which results the mixture of hexagonal and cubic phases [36] in Zn, Ni dual doped CdS nanostructures. Among the mixed phases of hexagonal and cubic structure, cubic phase is dominated than hexagonal. Dutkova et al. [39] also described that hexagonal phase of CdS was change-over to cubic phase during the addition of Zn = 10% ($Cd_{0.9}Zn_{0.1}S$). No extra peaks acquired in the XRD spectra confirm the absence of metal/oxide phases of Zn/Ni in the Cd-Zn-S lattice.

The substitution of Ni into Cd-Zn-S lattice not only replaces the Cd^{2+} ions and also survives as an interstitials in the Cd-S host lattice which creates more defect states within the system. The intensity reduction by Ni addition indicates the deterioration of crystalline nature. Moreover, the modulation in the position of XRD peaks and the intensity reduction reveals the proper substitution of Ni into $Cd_{0.9}Zn_{0.1}S$ structure. In addition, the induced structural disorder and the creation of defect associated sites are accountable for the alteration in XRD peak intensity and peak position [40].

The alteration in peak intensity, peak position (2θ), and FWHM (β) value along (111) plane, and d-value, cell parameter 'a', average crystallite size (D) and micro-strain (ε) of $Cd_{0.9}Zn_{0.1}S$ and $Cd_{0.89}Zn_{0.1}Ni_{0.01}S$ nanostructures is presented in Table 2. The mean crystallite size of the present system is estimated using Scherrer equation [41], $0.9 \ \lambda/\beta \ \cos\theta$, here $\lambda \approx 1.5406$ Å. The micro-strain (ε) of the current prepared system can be determined by the equation [42], $\beta \ \cos\theta/4$. The addition of Ni diminishes the size from 69 Å ($Cd_{0.9}Zn_{0.1}S$) to 43 Å and increases the strain from 5.005×10^{-3} ($Cd_{0.9}Zn_{0.1}S$) to 8.151×10^{-3}. The broadening of FWHM as well as the enhanced micro-strain are the additional reasons for the current decline in size. The noticed lattice parameter 'a' and the inter-planar distance 'd' are shifted to higher value by the addition of Ni into
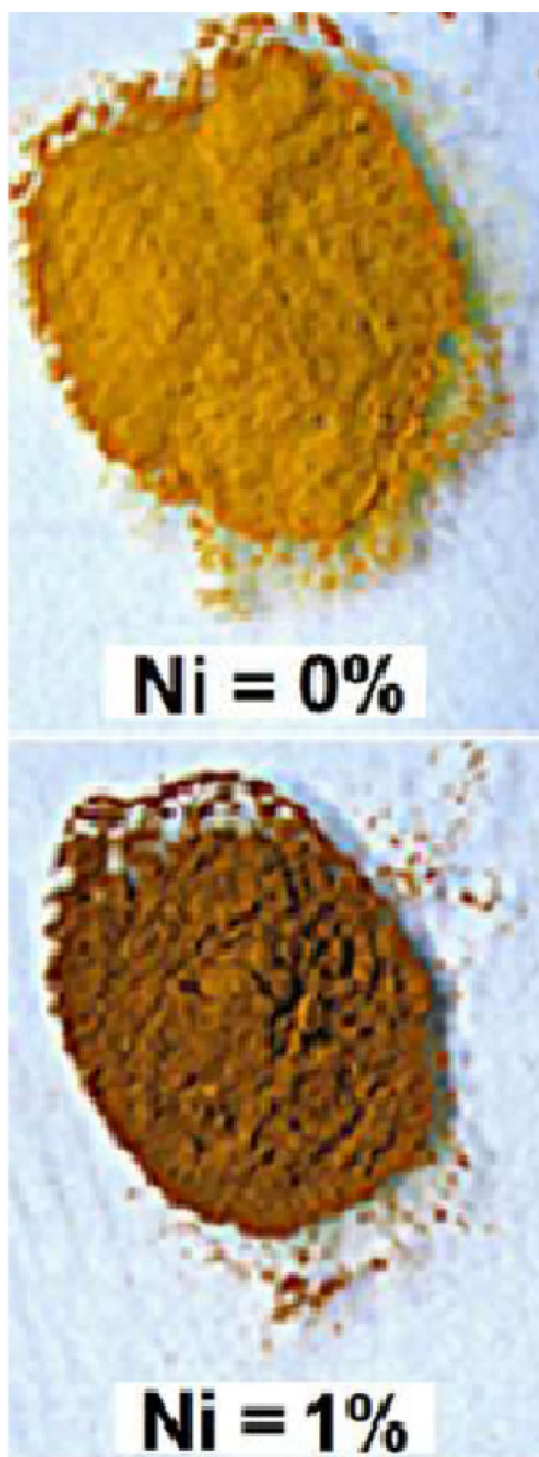
Fig. 2 The color of change of $Cd_{0.9}Zn_{0.1}S$ nanostructure from yellow to brown for Ni = 1% doped $Cd_{0.9}Zn_{0.1}S$

$Cd_{0.9}Zn_{0.1}S$ nanostructures. The similar increase of lattice constant and the shrinkage of size was supported by Woltersdorf et al. [43].

3.2 Microstructure and compositional studies

Figure 4a and b reveals the typical TEM micrographs $Cd_{0.9}Zn_{0.1}S$ and Ni-doped $Cd_{0.9}Zn_{0.1}S$ nanostructures, respectively. Figure 4a shows the TEM images of $Cd_{0.9}Zn_{0.1}S$ where the shape of the particles/grains are found to be nearly spherical in nature and they are tightly packed with smooth surface. The grains are well distributed within the sample with the mean size about 6 nm. Figure 4b shows TEM micrograph of $Cd_{0.89}Zn_{0.1}Ni_{0.01}S$ which possesses smaller size compared with $Cd_{0.9}Zn_{0.1}S$ nanostructure. The addition of Ni induces the lattice disorder and generates much defect associated states. There is no much change in shape of the grains except diminishing of size. The mean size of the Ni doped sample is around 4–5 nm.

In order to examine existence of Ni in Cd–Zn–S lattice, energy dispersive X-ray (EDX) studies have been executed over the whole samples as presented in Fig. 5b. Table 3 reveals the modification in quantitative examination of atomic % of the basic elements such as Cd, Zn, Ni and S in the synthesized samples using EDX analysis. The prominent and well-defined peaks confirm the presence of Cd, Zn, Ni and S in the prepared system. To improve the accuracy of measurement, the atomic level evaluation is carried out at various position of the samples with the help of EDX spectra. It is observed from Fig. 5 that Zn/ (Ni + Cd + Zn) ratio is found to be nearly 10% and the Ni/ (Ni + Cd + Zn) ratio is attained as 1.02% for Ni doped $Cd_{0.9}Zn_{0.1}S$. The results of Table 3 and Fig. 5 recommended that the ratio of the atomic % of the constitutional elements existing in the present samples coincidence with the quantity taken for the preparation of the samples.

3.3 Optical property

Optical absorption, transmittance and the band gap of the materials plays a significant role in the production and applications of opto-electronic devices. Figure 6 exposes the absorption spectra of $Cd_{0.9}Zn_{0.1}S$ and $Cd_{0.89}Zn_{0.1}Ni_{0.01}S$ nanostructures within the wavelength ranging from 300 to 550 nm. Zn = 10% doped CdS nanostructures display a strong optical absorption in the lower wavelength i.e., below 350 nm. The absorption comes down to very low at higher wavelength after exhibiting a remarkable fall

Fig. 3 XRD pattern of $Cd_{0.9}Zn_{0.1}S$ and Ni = 1% doped $Cd_{0.9}Zn_{0.1}S$ nanostructures between 20° and 60°
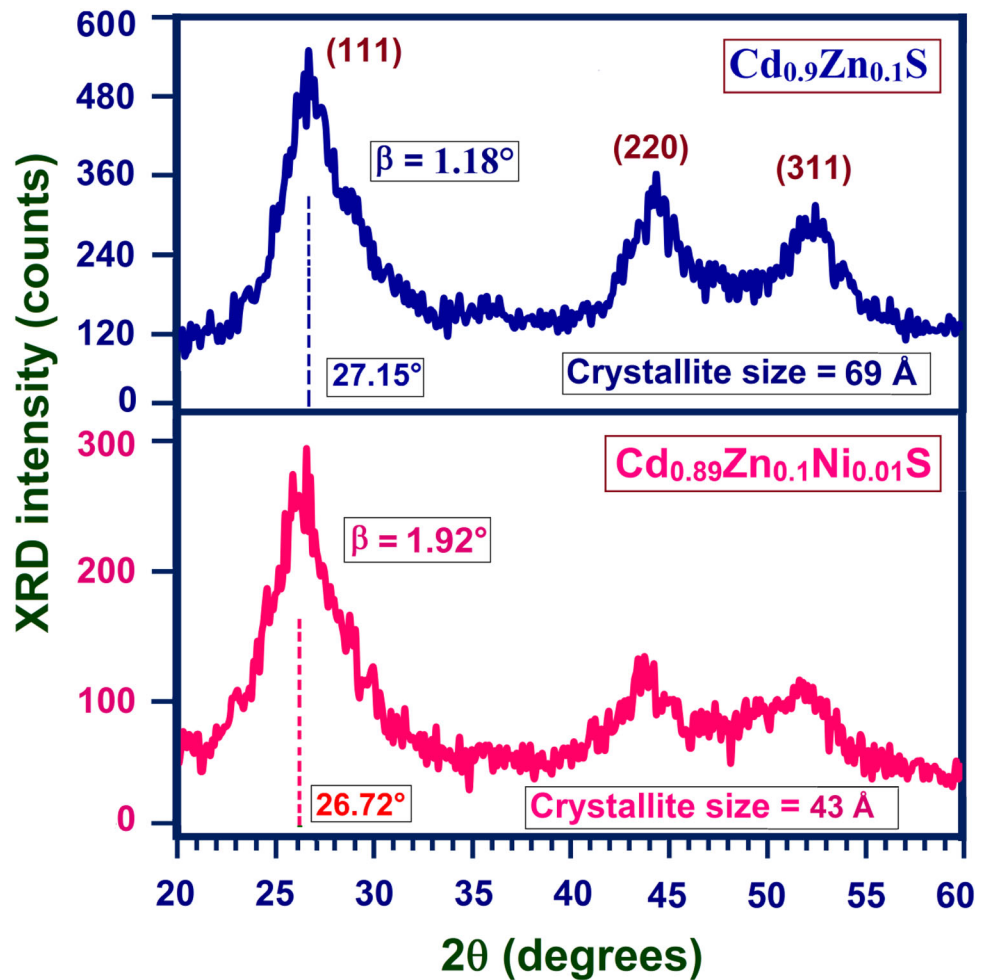

Table 2 The alteration in peak intensity, peak position (2θ), and FWHM (β) value along (111) plane, and d-value, cell parameter 'a', average crystallite size (D) and micro-strain (ε) of $Cd_{0.9}Zn_{0.1}S$ and $Cd_{0.89}Zn_{0.1}Ni_{0.01}S$ nanostructures

Samples	Peak intensity (counts)	Peak position (2θ) (°)	FWHM (β) (°)	d-value (Å)	Cell parameter a = b = c (Å)	Average crystallite size (D) (Å)	Micro-strain (ε) (10⁻³)
$Cd_{0.9}Zn_{0.1}S$	569	27.15	1.18	3.28 ± 0.01	5.68 ± 0.01	69	5.005
$Cd_{0.89}Zn_{0.1}Ni_{0.01}S$	397	26.72	1.92	3.33 ± 0.01	5.77 ± 0.01	43	8.151

down near band gap of the material. The addition of Ni shift the absorption edge along the higher wavelength region (red-shift). In addition to the red-shift of absorption edge, Ni added sample exhibits various anomalous absorption peaks around 321 nm, 354 nm (corresponding to UV region), and 438 nm corresponding to visible wavelength.

In general, the dominant UV absorption below 400 nm is originated from the transition of electrons between valence band and the conduction band which indicates the band gap of the materials [44]. More than one absorption peaks are noticed at Ni doped sample which is due to the creation of various defects such as interstitials, vacancies, etc. [45] by the inclusion of Ni impurity which work as trap centers and generate the anomalous peaks in absorption spectrum. The absorption peak around 438 nm in visible region at Ni added $Cd_{0.9}Zn_{0.1}S$ is owing to the existence of Cu/Zn interstitials in Cd–Ni–Zn–S lattice. The lattice disorder and the volume defects [40]

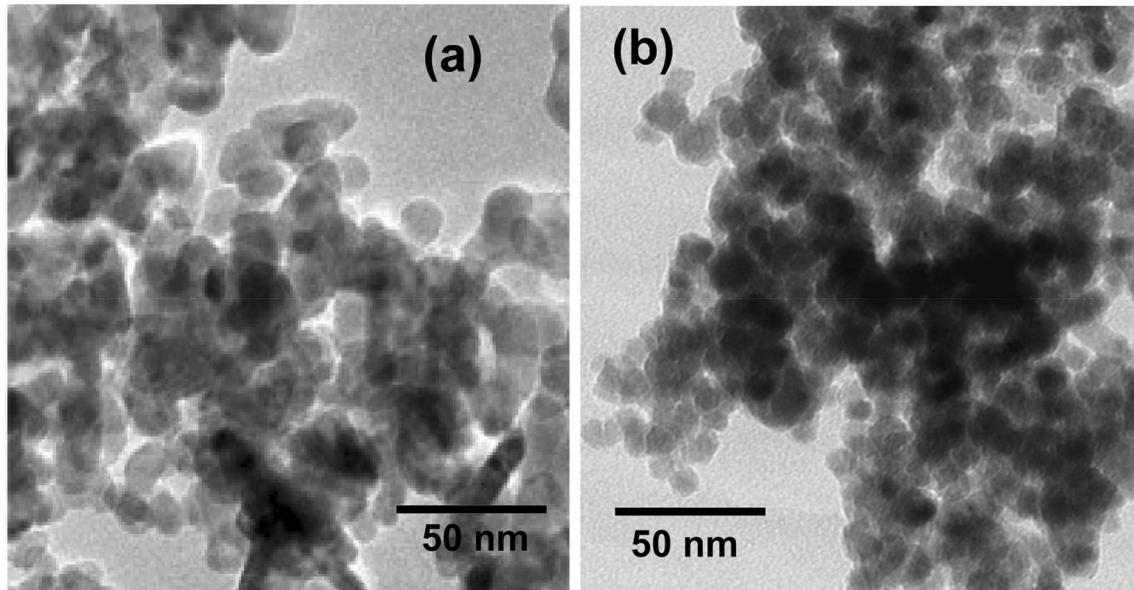**Fig. 4** SEM micrographs of **a** $Cd_{0.9}Zn_{0.1}S$ and **b** Ni = 1% doped $Cd_{0.9}Zn_{0.1}S$ nanostructures

stimulated by Ni produces some new inter-energy levels near conduction band and the transition between the inter valence - conduction band [46] may arise the visible absorption around 438 nm.

The band gap of $Cd_{0.9}Zn_{0.1}S$ and Ni-doped $Cd_{0.9}Zn_{0.1}S$ nanostructures is evaluated [42] by extrapolating the straight line of the graph of $(\alpha h\upsilon)^2$ versus the energy $(h\upsilon)$. Figure 7 represents the plot between $(\alpha h\upsilon)^2$ and $h\upsilon$ which is used to estimate the band gap of the material. The band gap the above two materials lies between 3.36 and 3.8 eV which have higher value than the micro-sized CdS (2.42 eV) [47]. The higher band gap noticed in the prepared samples is due to the formation of nano-sized particles/grains ($\approx$ 43–69 Å) which exhibits the better surface to volume ratio and smaller spatial dimension. The same trend of energy gap was reported in the literature [48, 49].

The band gap of $Cd_{0.9}Zn_{0.1}S$ is attained as 3.8 eV which is sharply decreased to 3.36 eV (ΔE_{g}- $\approx$ 0.44 eV) when Ni = 1% added into $Cd_{0.9}Zn_{0.1}S$. The similar shrinkage of band gap was reported by Senthil et al. [50] in Ni doped CdS. The addition of Ni^{2+} creates the free electrons named as "free carrier absorption" which is responsible for the current sharp decrease of band gap. The enhanced conductivity and the reduced resistance by Ni addition supports the free carrier absorption effect [28]. The one more reason for the decreasing band gap in Ni doped system is the strong interaction between 'p–d'

hybridization in Ni and 'p' state of sulfide which creates the intermediary impurity levels [51] inside the band gap. The current red-shift of band gap confirmed the proper inclusion of Ni^{2+} ions within Cd–Zn–S lattice [52]. Moreover, the reduction in E_g is associated with the defects which are induced by Ni and the localized energy states around the band edges as supported by Premarani et al. [53].

3.4 Fourier transform infrared (FTIR) studies

In order to confirm the presence of Cd, Zn, and Ni and occurrence of Cd/Zn/Ni–S bonds, FTIR spectra have been taken out between the wave numbers 400 to 4000 cm^{-1} at ambient temperature. Figure 8 reveals the FTIR spectra of $Cd_{0.9}Zn_{0.1}S$ and $Cd_{0.89}Zn_{0.1}Ni_{0.01}S$ nanostructures recorded with the help of KBr pellet method. The IR frequencies and their corresponding vibrational assignments of $Cd_{0.9}Zn_{0.1}S$ and $Cd_{0.89}Zn_{0.1}Ni_{0.01}S$ nanostructures at room temperature are presented in Table 4. The wide bands between 3200 and 3600 cm^{-1} signifies the stretching vibration of O-H [54] and sharp and high intensity peaks between 1500 and 1600 represents bending vibration of H-O-H which are present at the surface of the CdS [55].

The prominent band about 1410 cm^{-1} is owing to the symmetric and asymmetric stretching of carboxyl group (C=O) [56]. The feeble bands among

800–1100 cm^{-1} correspond to the microstructural changes associated with defect states formed by Ni or Zn through Cd-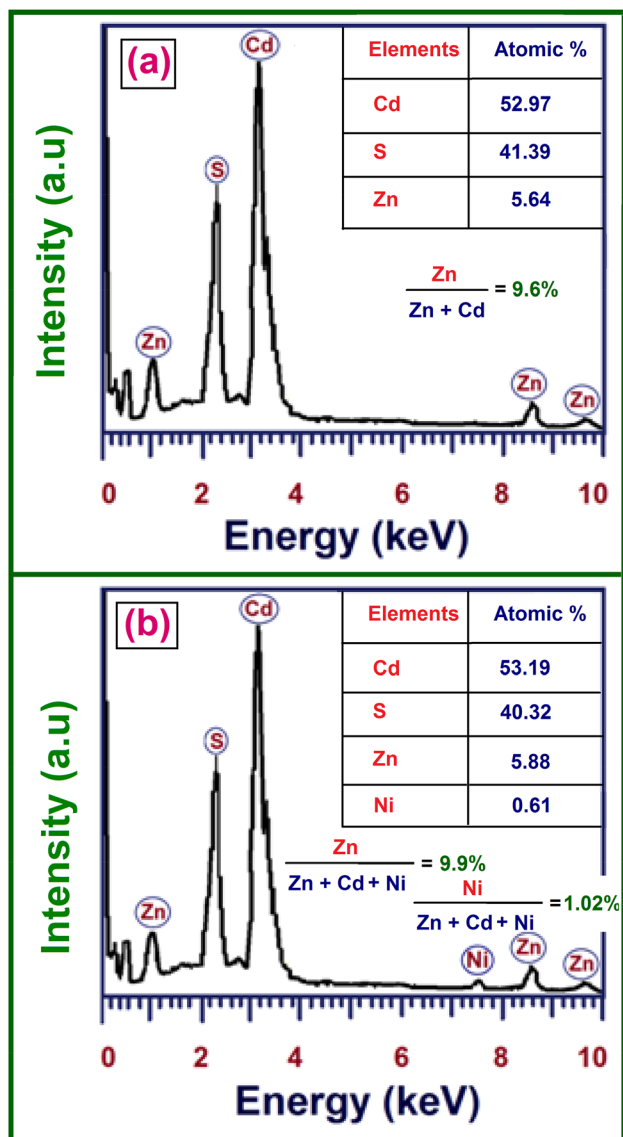S lattice. The bonding between metal and sulfur ions lies within 500–700 cm^{-1}. The characteristic bands around 662–671 cm^{-1} represents Cd-S stretching vibration [57]. The shift of characteristic band from 662 cm^{-1} (Ni = 0%) to 671 cm^{-1} for Ni = 1% addition indicates not only the reduction of size and also the proper inclusion of Ni^{+2} ions within the Cd–Zn–S lattice.

3.5 Photoluminescence (PL) studies

Figure 9 reveals the PL spectra of $Cd_{0.9}Zn_{0.1}S$ and $Cd_{0.89}Zn_{0.1}Ni_{0.01}S$ nanostructures between 350 and 640 nm. Zn-doped $Cd_{0.9}Zn_{0.1}S$ contains two different wide and broad range visible PL emissions. The first band centered at 402 nm corresponding to bluish-violet emission bands and the second band around 538 nm representing the green emission bands. Generally, the photoluminescence originated from either band to band transition i.e., by the recombination of electron and hole pairs or by the interaction
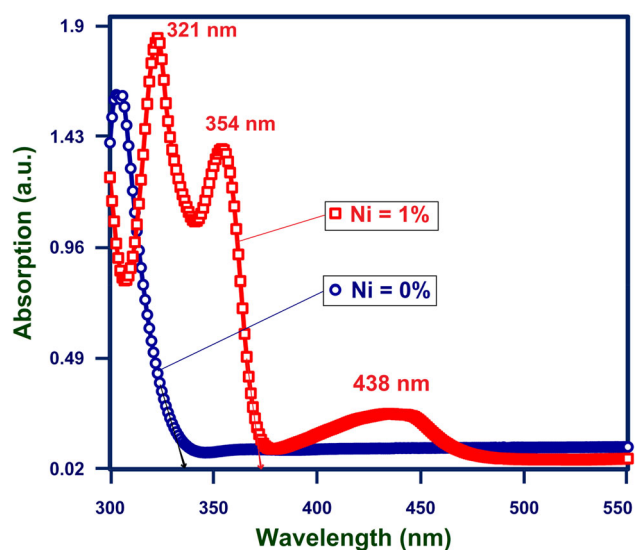

Fig. 5 Energy dispersive X-ray (EDX) spectra of **a** $Cd_{0.9}Zn_{0.1}S$ and **b** Ni = 1% doped $Cd_{0.9}Zn_{0.1}S$ nanostructures

Fig. 6 UV-Visible absorption spectra of Zn_0 $Cd_{0.9}Zn_{0.1}S$ and Ni = 1% doped $Cd_{0.9}Zn_{0.1}S$ nanostructures from 300 to 550 nm (Color figure online)

Table 3 The quantitative analysis of atomic percentage of the compositional elements presents in the $Cd_{0.9-x}Zn_{0.1}Ni_xS$ (x = 0 and 0.01) nanostructures using EDX analysis

Samples	Atomic % of the elements (%)				Zn/(Cd + Zn + Ni) ratio (%)	Ni/(Cd + Zn + Ni) ratio (%)
	b	S	Zn	Ni		
$Cd_{0.9}Zn_{0.1}S$	52.97	41.39	5.64	0	9.6	–
$Cd_{0.89}Zn_{0.1}Ni_{0.01}S$	53.19	40.32	5.88	0.61	9.9	1.02

between surface defect states i.e., the recombination of free charge carriers along the defect states [58]. The observed bluish-violet emission band is originated by the Cd^{2+} interstitials (I_{Cd}). The recombination of
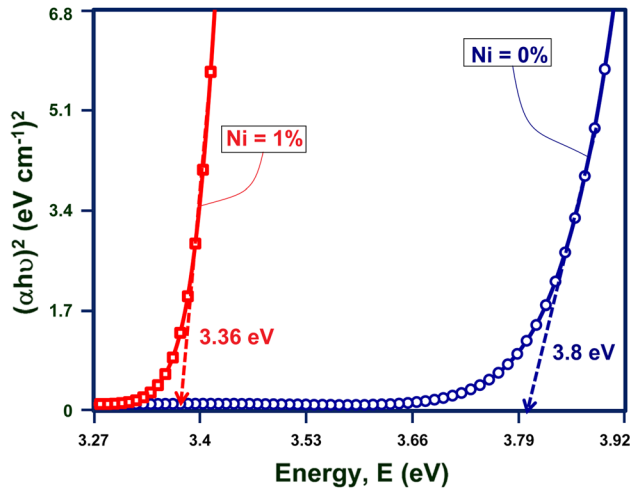
shallow region free electron and hole pair from I_{Cd} defect sites to the valence band causes the green emission band [59, 60].

The addition of Ni enhances both the bluish-violet and green emissions. The present enhanced emission intensity and the broadening effect is size dependent. The ionic radius of Ni^{2+} ions (≈ 0.069 nm) is lower than Cd^{2+} (0.097 nm) and Zn^{2+} (≈ 0.074 nm) ions and so the ionic bonding among Ni^{2+} and S^{2-} ions is superior than the other bondings such as among Cd^{2+} and S^{2-} [61]. Generally, Ni^{2+} sites can generate both acceptor and also donor type shallow states [62]. The noted green band emissions at 529–538 nm can be attributed to transitions between impurity levels inside the energy gap i.e, relating by the recombination of localized surface states [63]. Heitz et al. projected that electrons in the conduction band (CB) could be trapped by the energy level inside the CB via non-radiative transition owing to the distortion in the lattice generated by Ni doping and lastly combine with the holes in the VB via radiative transition [60]. The tuning of PL emissions in the visible wavelengths

Fig. 7 The $(\alpha h\upsilon)^2$ versus $h\upsilon$ curves of Zn_0 $Cd_{0.9}Zn_{0.1}S$ and Ni = 1% doped $Cd_{0.9}Zn_{0.1}S$ nanostructures for energy gap estimation

Fig. 8 FTIR spectra of Zn_0 $Cd_{0.9}Zn_{0.1}S$ and Ni = 1% doped $Cd_{0.9}Zn_{0.1}S$ nanostructures at room temperature in the wave number from 400 to 4000 cm^{-1} at room temperature
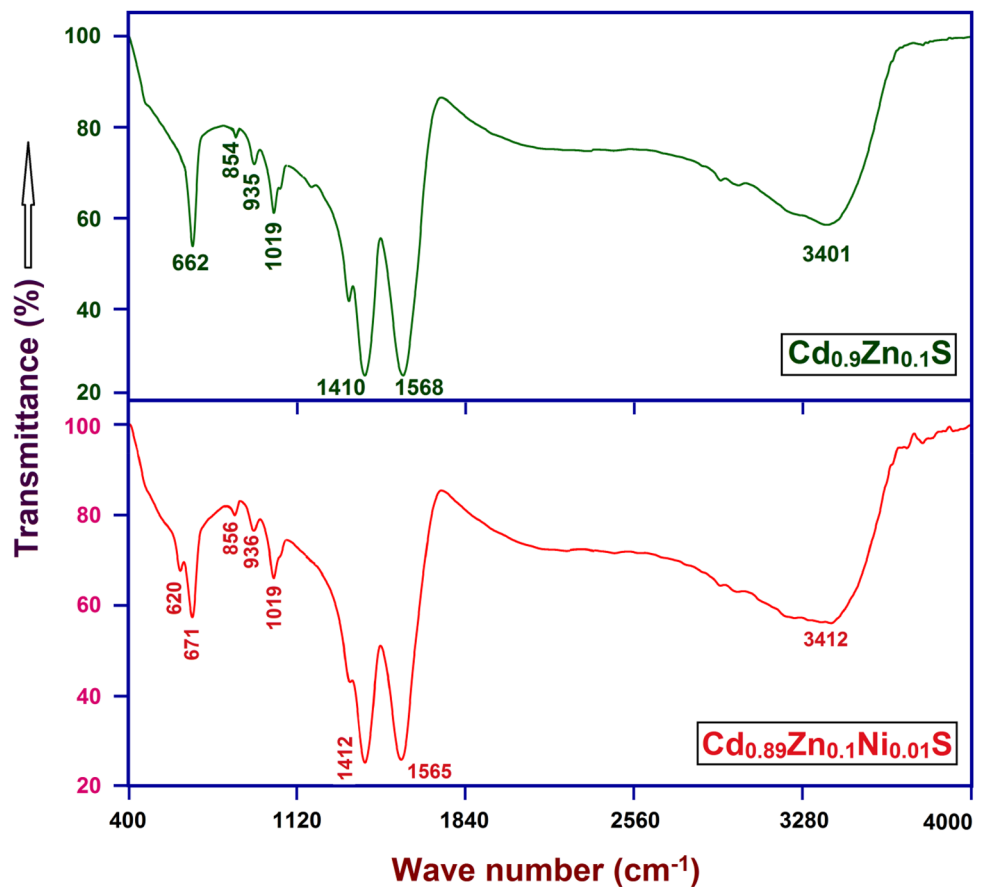
Table 4 IR peaks and their assignments of $Cd_{0.9}Zn_{0.1}S$ and $Cd_{0.89}Zn_{0.1}Ni_{0.01}S$ nanostructures obtained from FTIR investigation

Assignments	Wave number (cm^{-1})	
	$Cd_{0.9}Zn_{0.1}S$	$Cd_{0.89}Zn_{0.1}Ni_{0.01}S$
O–H stretching vibration of H_2O	3401	3412
H–O–H bending vibration	1568	1565
Vibration of C=O bonds	1410	1412
Micro-structural changes	854, 935, 1019	856, 936, 1019
Stretching mode of Cd-S	662	671, 620
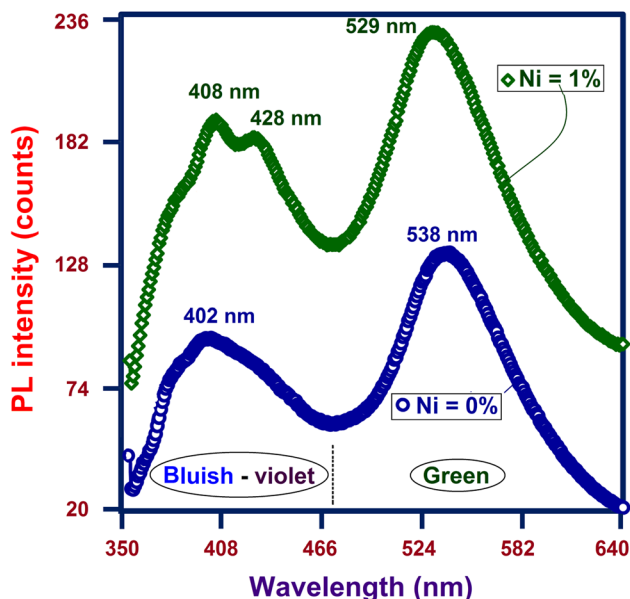
Fig. 9 The room temperature PL spectra of Zn_0 $Cd_{0.9}Zn_{0.1}S$ and Ni = 1% doped $Cd_{0.9}Zn_{0.1}S$ nanostructures between 350 and 640 nm

makes them as a potential material for opto-electronic applications.

3.6 Photocatalytic activity and stability studies

Methylene blue (MB) chemical is one of the primary water contaminants releasing from the industrial unit like textile factories. MB is a solid odorless, dark green colour powder which gives a blue colour solution during the dissolution with water at ambient temperature. The dye possesses high solubility in water and also harmful for the environment. In order to avoid the water contamination and ecological problem from the poisonous effluents like MB from textile wastage, single/dual TM doped CdS have been employed as photo-catalyst to remove the polluting substances. The addition of Zn^{2+} and Ni^{2+}

through Cd-S lattice acting an imperative role in altering the band structure of CdS and thus improves the efficiency of photo-catalytic behaviour of Zn and Ni added CdS nanostructures. In our work, the photo-catalytic removal behaviour of $Cd_{0.9}Zn_{0.1}S$ and $Cd_{0.89}Zn_{0.1}Ni_{0.01}S$ nanostructures have been evaluated using MB dye solution between the time intervals of 0-3 h and UV light is used as source. Based on the UV absorption spectra the characteristic wavelength of MB is found around 620-665 nm [64]. The photo-catalytic removal efficiency of any materials is depending upon the capacity of photo-generated electron-hole pair production [65].

The schematic graphical representation to describe the possible mechanism behind the photo-degradation of MB dye solution with the help of the present synthesized samples as catalyst under UV irradiation is displayed in Fig. 10. When Zn, Ni dual doped CdS are irradiated by UV light as revealed in Fig. 10, the electrons are easily excited from the valence level to the conduction level by liberating more free electrons and holes. Since, Ni exhibits partly filled orbital it can easily induces an electron donor level inside the band gap. The reduced energy gap by Ni addition in Cd-Zn-S lattice is the additional encouragement for the collection of exciting light and also for the creation of hole-electron pair [66]. The existence of sulfur vacancy, Zn^{2+} and Ni^{2+} ions in the Cd-S lattice modifies the band gap that delay the recombination rate of hole-electron pairs, which leads to enhance the photo-catalytic degradation of MB dye solution under UV irradiation [67].

The photo-induced electrons in CB can react with oxygen on the surface of CdS to create the superoxide free radical (O_2^-). The above anions react further with H_2O_2 and produce the hydroxyl radicals such as OH^-, $OH^.$ and O_2. The photo induced holes can be detained by OH^- and produce the hydroxyl radicals $OH^.$. The photo-induced strong $OH^.$ radicals and the superoxide free radicals (O_2^-) plays a great role in

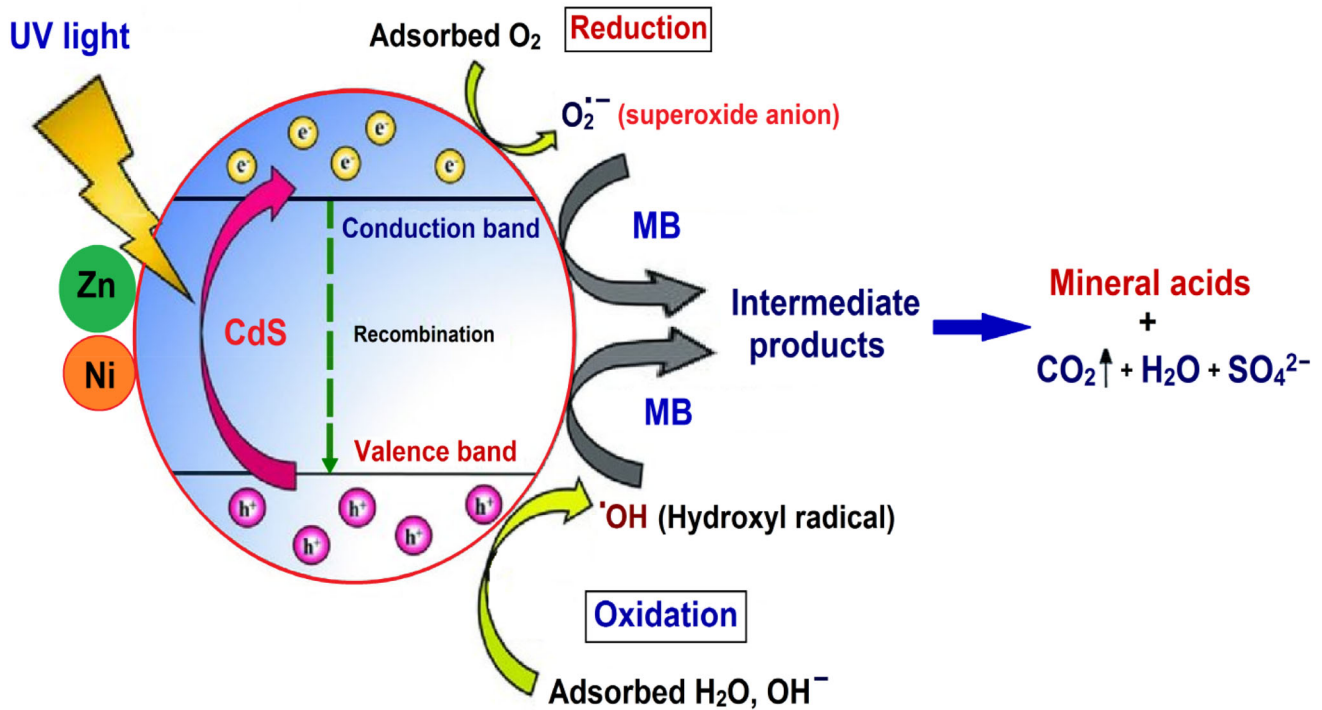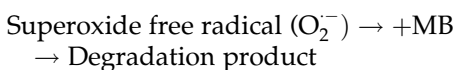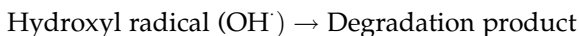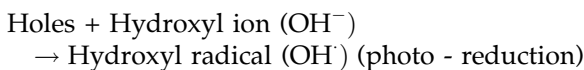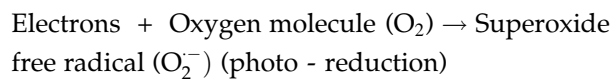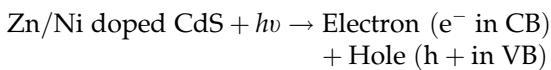**Fig. 10** The graphical representation of the photo-catalytic mechanism of Zn/Ni doped CdS nanostructures as a catalysts

degradation behaviour. They react with MB dye solution and break the all the chemical bonding and de-colorize the MB into colour-less form [68]. The degradation of MB using Zn/Ni doped CdS catalyst have been made by the subsequent reactions [69]:

$$Zn/Ni \text{ doped } CdS + h\upsilon \rightarrow \text{Electron } (e^- \text{ in CB}) \\ + \text{Hole } (h + \text{ in VB})$$

$$\text{Electrons } + \text{ Oxygen molecule } (O_2) \rightarrow \text{Superoxide} \\ \text{free radical } (O_2^{\cdot-}) \text{ (photo - reduction)}$$

$$\text{Holes } + \text{ Hydroxyl ion } (OH^-) \\ \rightarrow \text{Hydroxyl radical } (OH^{\cdot}) \text{ (photo - reduction)}$$

$$\text{Hydroxyl radical } (OH^{\cdot}) \rightarrow \text{Degradation product}$$

$$\text{Superoxide free radical } (O_2^{\cdot-}) \rightarrow +MB \\ \rightarrow \text{Degradation product}$$

After completion of the photo-degradation reaction, the solution of MB dye is dis-integrated into CO_2, H_2O and SO_4^{2-}.

Figure 11 reveals the optical absorption of MB dye using $Cd_{0.9}Zn_{0.1}S$ and $Cd_{0.89}Zn_{0.1}Ni_{0.01}S$ nanostructures as a photo-catalyst for different irradiation times from 0 to 3 h. In both cases, the optical absorption falls down drastically with increase of irradiation time. In the entire measurement, MB solution without any catalyst is consider as a control. The reduction of absorption intensity is maximum for $Cd_{0.89}Zn_{0.1}Ni_{0.01}S$ sample compared with $Cd_{0.9}Zn_{0.1}S$. For the purpose of getting more idea about the disintegration of MB dye, a graph between the concentration ratio (C_t/C_0) of MB and light exposure time between 0-3 h have been taken for MB dye solution, $Cd_{0.9}Zn_{0.1}S$ and $Cd_{0.89}Zn_{0.1}Ni_{0.01}S$ samples and the plot is illustrated in Fig. 12a. Figure 12b represents the degradation efficiency of MB dye solution, $Cd_{0.9}Zn_{0.1}S$ and $Cd_{0.89}Zn_{0.1}Ni_{0.01}S$ samples for various irradiation times from 0 h to 3 h. The degradation efficiency (η) can be derived by the following relation [70], η (%) = $[(C_0–C_t)/C_0] \times 100 = [(A_0–A_t)/A_0] \times 100$ where, C_0 and C_t are concentration of the dye at the irradiation for time, '0' and 't' minutes, respectively, and A_0 and A_t are the corresponding absorption values.

Generally, the value of degradation efficiency is based on the morphological changes and size of the catalyst particles / grains [71]. It is noteworthy that the Ni added $Cd_{0.9}Zn_{0.1}S$ sample illustrates the improved photocatalytic behaviour than that of $Cd_{0.9}Zn_{0.1}S$ sample. The above result recommends that the inclusion of Ni^{2+} ions improved the dye
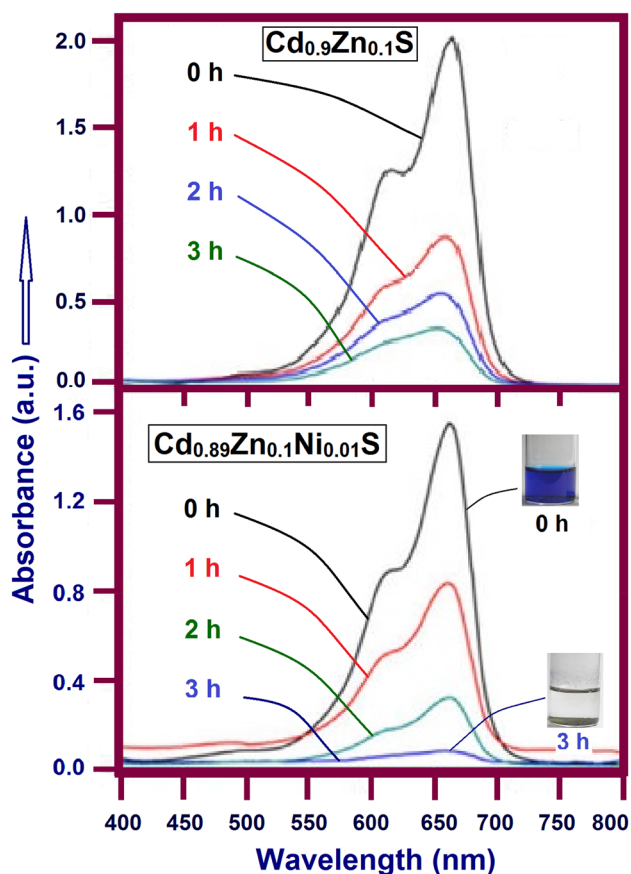
Fig. 11 The variation of absorption intensity of MB solution using $Cd_{0.9}Zn_{0.1}S$ and Ni = 1% doped $Cd_{0.9}Zn_{0.1}S$ nanostructures as a catalysts as a function of wavelength from 400 to 800 nm

removal capacity of CdS nanostructures significantly than $Cd_{0.9}Zn_{0.1}S$ which is owing to the diminishing size and the enhanced surface to volume ratio. The improved surface to volume ratio increases the active sites and so a huge amount of MB dye molecules can interact through the surface of the spherical nanostructures, ensuring better photo-catalytic dye removal capacity [72]. Figure 12c illustrates the transformation of colour of MB dye from blue (0 h) to transparent white at 3 h irradiation time using Ni-doped $Cd_{0.9}Zn_{0.1}S$ powder as a photo-catalyst. The observed maximum dye removal capacity using Ni-doped $Cd_{0.9}Zn_{0.1}S$ catalyst is the combined effect of more charge carriers liberation, better absorbance along the visible wavelength, surface area enhancement and the creation of new defect associated states [73].

In addition to the dye removal capacity, the re-usability of the catalyst is also most significant one to improve the stability of the material for the practical
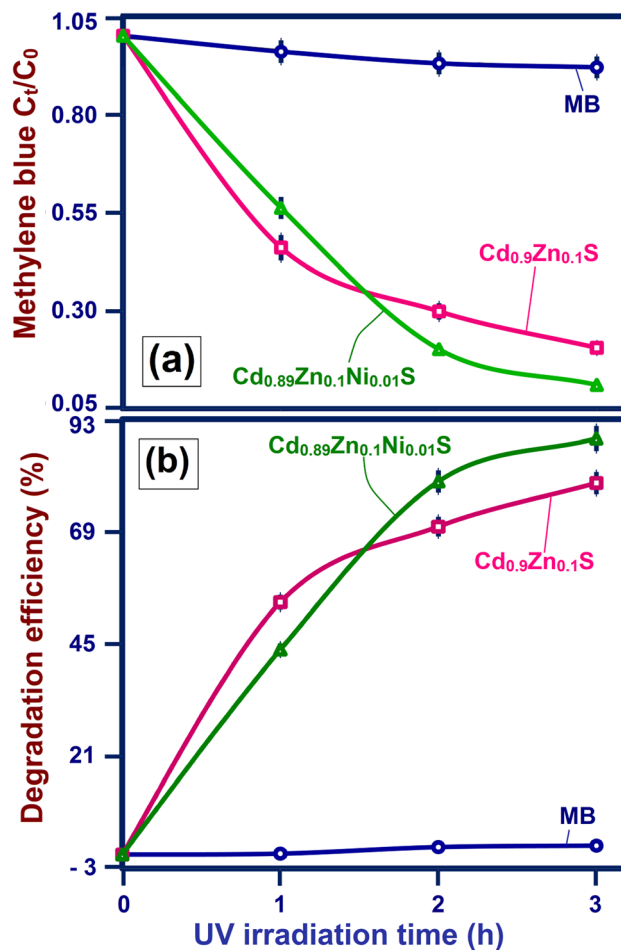
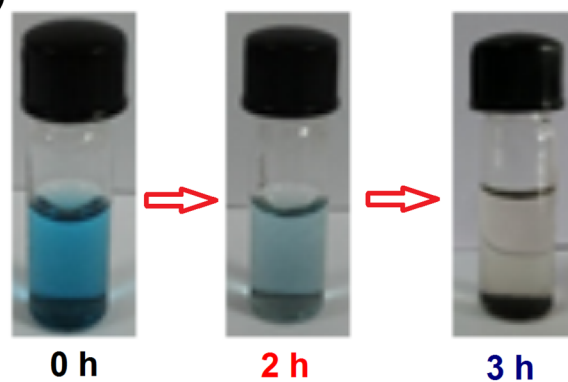**Fig. 12 a** The concentration versus irradiation time profile (0–3 h) and **b** degradation efficiency of MB of $Cd_{0.9}Zn_{0.1}S$ and Ni = 1% doped $Cd_{0.9}Zn_{0.1}S$ nanostructures and **c** colour change from blue (0 h) to transparent colour at 3 h of Zn, Ni co-doped CdS (Color figure online)

usage in industry. Therefore, Ni-doped $Cd_{0.9}Zn_{0.1}S$ is taken as catalyst for the further re-cycling process with UV light as a source and effective outcome is displayed as shown in Fig. 13. At the end of each

cycle, the collected sample is washed many times using de-ionized water and dehydrated with the help of oven at 70 °C for 1 h. Now, the cleaned sample was used once again for the consequent degradation. The disintegration percentage is found to be 89 at the first cycle which is reduced to 70% at 6th repeated cycle. Figure 13 shows the progressive decrement in photo-catalytic activity over six repeated cycles and the loss of degradation rate is ~ 19% after six cycles. The possible reasons for the present decrease in the photo-catalytic behaviour may be owing to the loss of catalysts by the drying and washing. The outcome of this activity indicates that Ni-doped $Cd_{0.9}Zn_{0.1}S$ possesses better dye removal capacity and stability even after 6 repeated cycles.

3.7 Antibacterial studies

The anti-bacterial behaviour of $Cd_{0.9}Zn_{0.1}S$ and $Cd_{0.89}Zn_{0.1}Ni_{0.01}S$ nanostructures against the bacterial pathogens like *S.aureus* (gram positive) and *E. coli* (gram negative) have been carried out to study the micro-organism killing efficiency. Figure 14 reveals the zone of inhibition (ZOI) of $Cd_{0.9}Zn_{0.1}S$ and $Cd_{0.89}Zn_{0.1}Ni_{0.01}S$ in mm against *S.aureus* and *E. coli* where norfloxin is used as a standard. Figure 15 shows a typical graphical demonstration of ZOI for different bacterial pathogens like *S.aureus* and *E. coli*. Ni - doped $Cd_{0.9}Zn_{0.1}S$ shows the better anti-bacterial behaviour against the bacterial strains than $Cd_{0.9}Zn_{0.1}S$ which is preferably due to the variation in the quality of the bacterial cell walls.
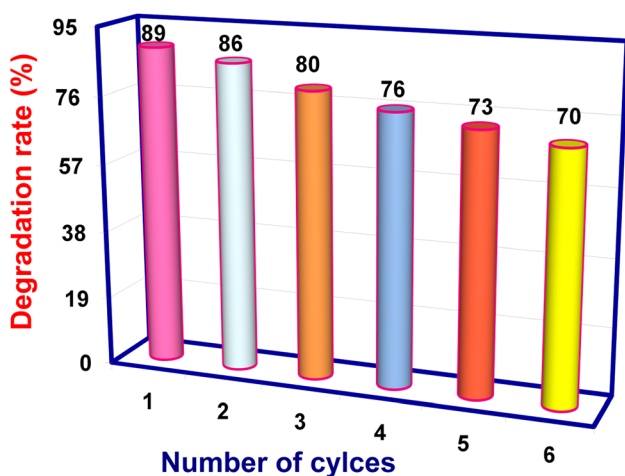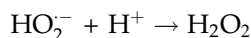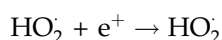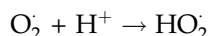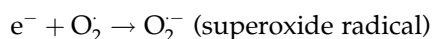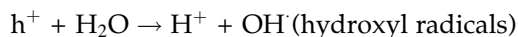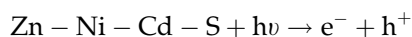

Fig. 13 Recycled photo-catalytic activity testing of Zn, Ni co-doped CdS for degradation of MB under UV irradiation (3 h irradiation time) for sex cycles of degradation reaction

Even though various mechanisms [74, 75] have been proposed to explain the anti-bacterial behaviour of the synthesized samples, the dis-integration of CdS and the reactive oxygen species (ROS) generation are considered as the foremost mechanism. The ROS such as O_2^-, $OH^.$, and H_2O_2 [76–78] are produced during the electron transition between VB and CB. The creation of ROS are as follows:

$$Zn - Ni - Cd - S + h\upsilon \rightarrow e^- + h^+$$

$$h^+ + H_2O \rightarrow H^+ + OH^. (hydroxyl\ radicals)$$

$$e^- + O_2 \rightarrow O_2^{.-} (superoxide\ radical)$$

$$O_2^. + H^+ \rightarrow HO_2^.$$

$$HO_2^. + e^+ \rightarrow HO_2^.$$

$$HO_2^- + H^+ \rightarrow H_2O_2$$

The $OH^.$ and $O_2^{.-}$ are the powerful ROS species to prevent the development of bacterial cells and they produce intense toxicity to the bacterial strains. Padmavathy well as Vijayaraghavan [79] reported that the ROS species such as $OH^.$ radicals and O_2^- radicals influence the external segment of the bacterial cellular membrane and the H_2O_2 can move in to the inner segment of bacterial cells. The mechanism to explain the antibacterial behaviour of Zn, Ni doped CdS nanostructures is as shown in Fig. 16. It is noticed from Figs. 14 and 15 that within $Cd_{0.9}Zn_{0.1}S$ and $Cd_{0.89}Zn_{0.1}Ni_{0.01}S$ nanostructures, Ni doped sample exhibits better anti-bacterial activity.

The noticed higher bacterial killing ability at Ni doped system is due to the lower grain size and also higher ROS producing capacity. The reduced size enhances the surface-to-volume ratios and improve the combination with biological pathogens [80]. The presence of ROS speeds up the dis-association of cell walls which causes the leakage of cell elements and induce the ultimate cell death [81] as shown in Fig. 16. In addition, the growth of bacterial strains is decreased by releasing the metal ions such as Zn^{2+}, Cd^{2+} and Ni^{2+}. These positive charged metal ions are attracted by the negative charged bacterial cells and so the metal ions easily penetrate the bacterial cell walls and react with—SH groups in the cells which leads the death of the microbes [70].

The observed ZOI from Fig. 15 that gram negative bacterial strain exhibit higher antibacterial activity than gram positive. Although many bacterial strains have internal cell wall, gram-negative strains hold a
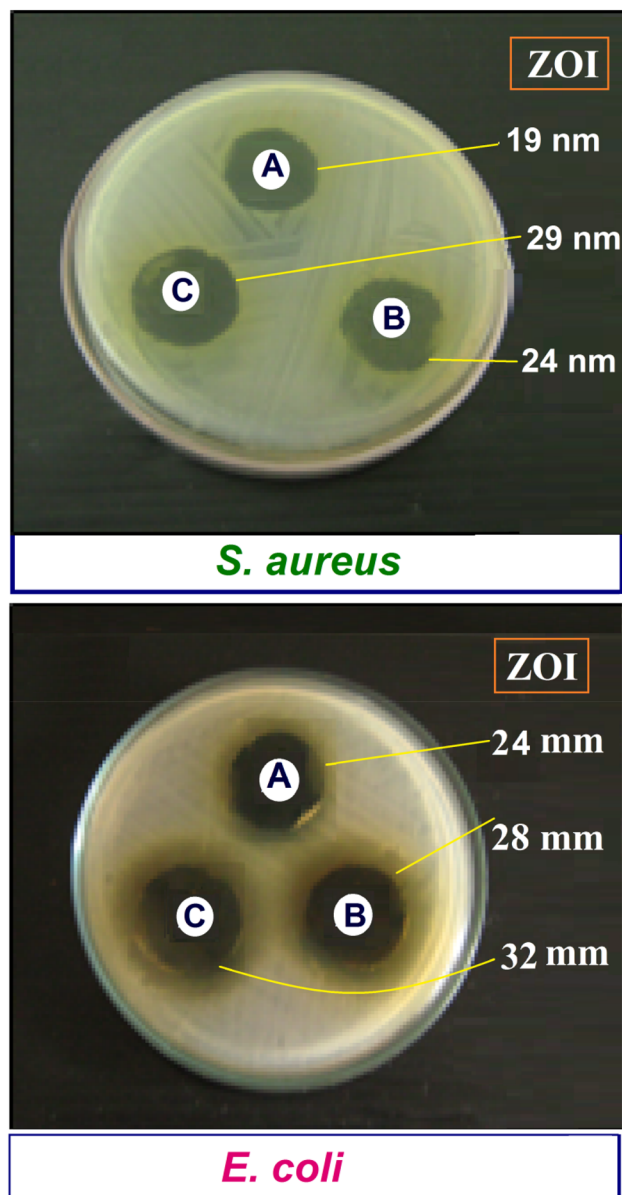
Fig. 14 The zone of inhibition (ZOI) in mm of $Cd_{0.9}Zn_{0.1}S$ and Ni = 1% doped $Cd_{0.9}Zn_{0.1}S$ nanostructures against *S. aureus* and *E. coli* bacterial strains

Fig. 15 The graphical representation of ZOI for different microorganisms such as *S. aureus* and *E. coli* bacterial strains

bacteria. Vanaja et al. [82] described that gram negative strains exhibited thin and multi-layered lipid materials in the cell wall, and hence the particles simply enter into bacterial strain and then revealed the higher inhibition zone than the gram positive bacterial strains.

4 Conclusions

Following are the conclusions drawn from the present investigation:

- Controlled synthesis of $Cd_{0.9}Zn_{0.1}S$ and $Cd_{0.89}Zn_{0.1}Ni_{0.01}S$ nanostructures by chemical co-precipitation route have been reported.
- The XRD analysis confirmed the cubic structure of CdS on Zn doping and Zn, Ni dual doping without any secondary/impurity phases and no alteration in cubic CdS phase was noticed by Zn/Ni addition.
- The shrinkage of crystallite size from 69 to 43 Å and the variation in lattice constants and microstrain were described by the addition of Ni and the defects associated with Ni^{2+} ions.
- The enhanced optical absorbance in the visible wavelength and the reduced energy gap by Ni substitution showed that $Cd_{0.89}Zn_{0.1}Ni_{0.01}S$

unique external cell wall which prohibit various drugs and antibiotics and reduce the cell damage. This extraordinary external cell wall in the gram negative strains is responsible for getting more antibacterial opposing capacity than gram-positive
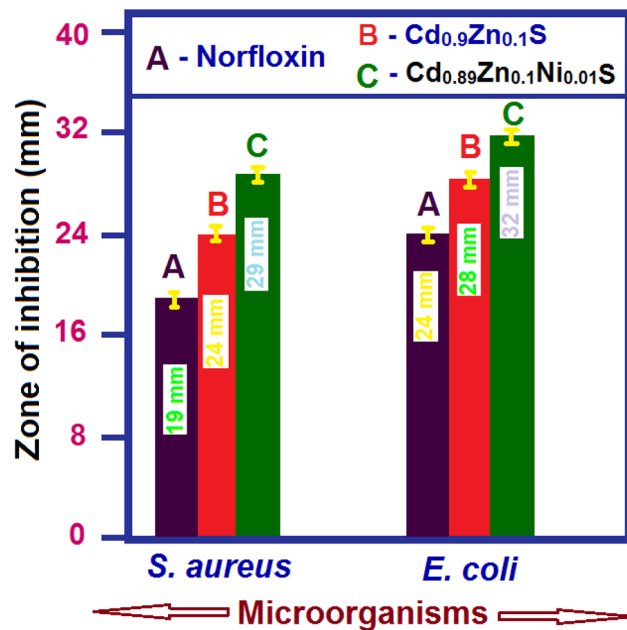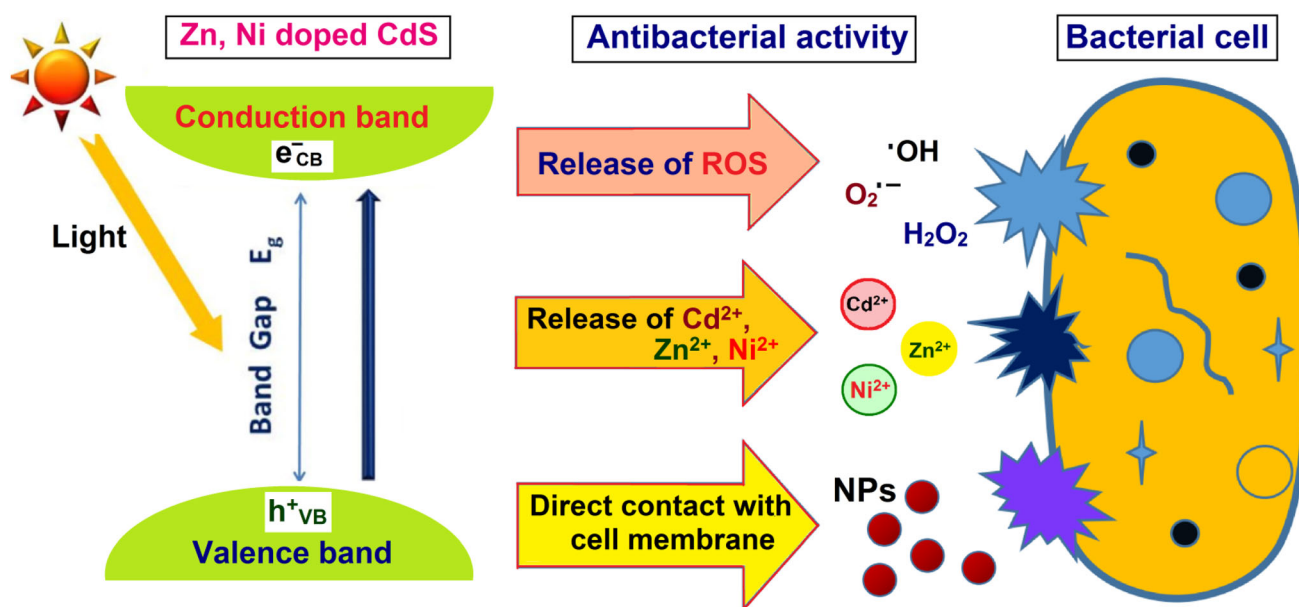
Fig. 16 The graphical representation of mechanism behind the antibacterial activity of Ni = 1% doped $Cd_{0.9}Zn_{0.1}S$ nanostructures

nanostructures are useful to improve the efficiency of opto-electronic devices.

- The functional groups of Cd-S/Zn-Cd+-S/Zn/Ni-Cd-S and their chemical bonding were verified by Fourier transform infrared studies.
- The elevated visible PL emissions such as blue and green emissions by Ni addition was explained by decreasing of crystallite size and generation of more defects.
- Zn, Ni dual doped CdS nanostructures are identified as the probable an efficient photo-catalyst for the degradation of methylene blue dye.
- The liberation of more charge carriers, better visible absorbance, improved surface to volume ratio and the creation of more defects are accountable for the current photo-catalytic activity in Zn/Ni doped CdS which exhibited better photo-catalytic stability after sex cycling process.
- The better bacterial killing ability is noticed in Ni doped $Cd_{0.9}Zn_{0.1}S$ nanostructure which is due to the collective effect of lower particle/grain size and also higher ROS producing capacity.

References

1. G.F. Zheng, W. Lu, C.M. Lieber, Adv. Mater. **21**, 1890–1893 (2004)
2. Y. Huang, H.F. Duan, C.M. Lieber, Small **1**, 142–147 (2005)
3. M. Ueta, H. B. Kanzaki, K. Kobayashi, Y. Toyozawa, E. Hanamura, Excitonic processes in solids, In: Springer Series in Solid State Sciences, Vol. 60, Springer, Berlin (1986)
4. A.H. Mueller, M.A. Petruska, M. Achermann, D. Werder, E. Akhadov, D. Koleske, M. Hoffbauer, V.I. Klimov, Nano Lett. **5**(6), 1039–1044 (2005)
5. N. Romeo, A. Bosio, A. Romeo, Sol. Energy Mater. Sol. Cells **94**, 2–7 (2010)
6. Z.K. Heiba, M.B. Mohamed, N.G. Imam, J. Mol. Struct. **1136**, 321–329 (2017)
7. N.G. Imam, M.B. Mohamed, J. Mol. Struct. **1105**, 80–86 (2016)
8. R. Ochoa-Landin, J. Sastre-Hernandez, O. Vigil-Galan, R. Ramirez-Bon, Sol. Energy **84**, 208–214 (2010)
9. C. Voss, S. Subramanian, C.-H. Chang, J. Appl. Phys. **96**, 5819 (2004)
10. N.R. Paudel, K.A. Wieland, A.D. Compaan, Sol. Energy Mater. Sol. Cells **105**, 109–112 (2012)
11. P. Elavarthi, A.A. Kumar, G. Murali, D.A. Reddy, K.R. Gunasekhar, J. Alloys Compd. **656**, 510–517 (2016)
12. M.B. Mohamed, M.H. Abdel-Kader, A.A. Alhazime, J.Q.M. Almarashi, J. Mol. Struct. **1155**, 666–674 (2018)
13. D. Mocatta, G. Cohen, J. Schattner, O. Millo, E. Rabani, E. Rabani, U. Banin, Science **332**, 77–81 (2011)
14. R. Beaulac, L. Schneider, P.I. Archer, G. Bacher, D.R. Gamelin, Science **325**, 973–976 (2009)
15. O. Lehmann, K. Kompe, M. Haase, J. Am. Chem. Soc. **126**, 14935–14942 (2004)
16. L. Zu, D.J. Norris, T.A. Kennedy, S.C. Erwin, A.L. Efros, Nano Lett. **6**, 15334 (2006)

17. X. Huang, A. Makmal, J.R. Chelikowsky, L. Kronik, Phys. Rev. Lett. **94**, (2005)

18. P. Chand, R. Ghosh, Sukriti. Optik **161**, 44–53 (2018)

19. M.V. Artemyev, V. Sperling, U. Woggon, J. Appl. Phys. **81**(10), 6975 (1997)

20. V. Narasimman, V.S. Nagarethinam, K. Usharani, A.R. Balu, Int. J. Thin. Films Sci. Tec. **5**, 17–24 (2016)

21. H. Sekhar, D.N. Rao, J. Mater. Sci. **47**, 1964–1971 (2012)

22. M. Anpo, M. Takeuchi, J. Catal. **216**, 505–516 (2003)

23. I. Devadoss, S. Muthukumaran, M. Ashokkumar, J. Mater. Sci. **25**, 3308–3317 (2014)

24. S. Jothia, R.K. Seenivasanb, S. Muthukumaran, Surf. Interfaces **14**, 215–221 (2019)

25. R. Chauhan, A. Kumar, R.P. Chaudhary, Appl. Surf. Sci. **270**, 655–660 (2013)

26. S.M. Taheri, M.H. Yousefi, A.A. Khosravi, Braz. J. Phys. **40**, 301–305 (2010)

27. S.K. Mishra, R.K. Srivastava, S. Prakash, R.S. Yadav, A. Panday, J. Alloys Compd. **513**, 118–124 (2012)

28. A. Rmili, F. Ouachtari, A. Bouaoud, A. Louardi, T. Chtouki, B. Elidrissi, H. Erguig, J. Alloys Compd. **557**, 53–59 (2013)

29. S. Chandramohan, A. Kanjilal, J.K. Tripathi, S.N. Sarangi, T. Sathyamoorthy, T. Som, J. Appl. Phys. **05**, (2009)

30. B.S. Rao, V.R. Reddy, B.R. Kumar, T.S. Ao, Int. J. Nanosci. **11**, 1240006 (2012)

31. R. Singh, S. Basu, B. Pal, Mater. Res. Bull. **94**, 279–286 (2017)

32. D.E. Aimouch, S. Meskine, A. Birsan, V. Kuncser, A. Zaoui, A. Boukortt, Mater. Chem. Phys. **213**, 249–258 (2018)

33. A. Firdous, D. Singh, M.M. Ahmad, Appl. Nanosci. **3**, 13–18 (2013)

34. G. Rajkumar, M. Rajkumar, V. Rajendran, S. Aravindan, J. Am. Ceram. Soc. **94**, 2918–2925 (2011)

35. N. Lenin, K. Sakthipandi, R.R. Kanna, G. Rajkumar, Ceram. Int. **44**(2018), 21866–218663 (1873)

36. A.V.G. Devi, G. Rajkumar, K. Sakthipandi, V. Rajendran, N. Rajendran, Phosphorus Sulfur Silicon Relat. Elem. **187**, 1434–1449 (2012)

37. G. Rajkumar, V. Dhivya, S. Mahalaxmi, K. Rajkumar, G.K. Sathishkumar, J. Non-cryst, Solids **493**, 108–118 (2018)

38. Z. Sedaghat, N. Tagavinia, M. Marandi, J. Nanotechnol. **17**, 3812 (2006)

39. E. Dutkova, P. Balaz, P. Pourghahramani, A.V. Nguyen, V. Sepelak, A. Feldhoff, J. Kovac, A. Satka, Solid State Ion. **179**, 1242–1245 (2008)

40. X.L. Yang, Z.T. Chen, C.D. Wang, Y. Zhang, X.D. Pei, Z.J. Yang, G.Y. Zhang, Z.B. Ding, K. Wang, S.D. Yao, J. Appl. Phys. **105**, (2009)

41. B.D. Cullity, *Elements of X-ray Diffraction* (Addison Wesley, USA, 1978)

42. S. Anandan, S. Muthukumaran, M. Ashokkumar, Superlatt. Microstruct. **74**, 247–260 (2014)

43. J. Woltersdorf, A. Nepijko, E. Pippel, Surf. Sci. **106**, 64–69 (1981)

44. I. Devadoss, P. Sakthivel, S. Muthukumaran, N. Sudhakar, Ceram. Int. **45**, 3833–3838 (2019)

45. S. Chandramohan, T. Strache, S.N. Sarangi, R. Sathyamoorthy, T. Som, Mater. Sci. Eng. B **171**, 16–19 (2010)

46. .M. Fox, Optical Properties of Solids, Oxford University Press, 2001

47. K.S. Kumar, A. Divya, P.S. Reddy, Appl. Surf. Sci. **257**, 9515–9518 (2011)

48. M. Elango, K. Gopalakrishnan, S. Vairam, M. Thamilselvan, J. Alloys Compd. **538**, 48–55 (2012)

49. C.S. Tiwary, R. Sarkar, P. Kumbhakar, A.K. Mitr, Phys. Lett. A **372**, 5825–5830 (2008)

50. K. Senthil, D. Mangalaraj, S.K. Narayandass, B. Hong, Y. Roh, C.S. Park, J. Yi, Sci. Technol. **17**, 97–103 (2002)

51. M.A. Kamran, R.B. Liu, L.J. Shi, B.S. Zou, J. Phys. Chem. C **117**, 17777–17785 (2013)

52. M. Thambidurai, N. Muthukumarasamy, S. Agilan, N.S. Arul, N. Murugan, R. Balasundaraprabhu, J. Mater. Sci. **46**, 3200–3206 (2011)

53. R. Premarani, J.J. Devadasan, S. Saravanakumar, R. Chandramohan, T. Mahalingam, J. Mater. Sci. **26**, 2059–2065 (2015)

54. Z.R. Khan, M. Zulfequar, M.S. Khan, Mater. Sci. Eng., B **174**, 145–149 (2010)

55. J. Liu, C. Zhao, Z. Li, J. Chen, H. Zhou, S. Gu, Y. Zeng, Y. Li, Y. Huang, J. Alloys Compd. **509**, 9428–9433 (2011)

56. S. Senthilkumaar, K. Rajendran, S. Banerjee, T.K. Chini, V. Sengodan, Mater. Sci. Semi. Process **11**, 6–12 (2008)

57. M.F. Kotkata, A.E. Masoud, M.B. Mohamed, E.A. Mahmoud, Physica E **41**, 1457–1465 (2009)

58. X. Sun, X. Ma, L. Bai, J. Liu, Z. Chang, D.G. Evans, X. Duan, J. Wang, J.F. Chiang, Nano Res. **4**, 226–232 (2011)

59. M. Muthusamy, S. Muthukumaran, M. Ashokkumar, Ceram. Int. **40**, 10657–10666 (2014)

60. R. Heitz, A. Hoffmann, I. Broser, Phys. Rev. B **48**, 8672–8682 (1993)

61. M. Ashokkumar, S. Muthukumaran, J. Lumin. **145**, 167–174 (2014)

62. A. Heitz, I. Hoffmann, Broser. Phys. Rev. B **49**, 14307 (1994)

63. H. Huang, X. Han, X.W. Li, S. Wang, P.K. Chu, Y. Zhang, A.C.S. Appl, Mater. Interfaces **7**, 482–492 (2015)

64. R. Atchudan, T.N.J.I. Edison, S. Perumal, D. Karthikeyan, Y.R. Lee, J. Photochem. Photobiol. B **162**, 500–510 (2016)

65. C.B. Ong, L.Y. Ng, A.W. Mohammad, Renew. Sustain. Energy Rev. **81**, 536–551 (2018)

66. R.M. Navarro, M.C. Alvarez-Galvan, J.A.V. de la Mano, S.M. Al-Zahranib, J.L.G. Fierroa, Energy Environ. Sci. **3**, 1865–1882 (2010)

67. B. Ahmed, A.K. Ojha, S. Kumar, Spectrochim. Acta A Mol. Biomol. Spectrosc. **179**, 144–154 (2017)

68. K. Thongsuriwong, P. Amornpitoksuk, S. Suwanboon, J. Sol-Gel. Sci. Technol. **62**, 304–312 (2012)

69. A. Ali, X. Zhao, A. Ali, L. Duan, H. Niu, C. Peng, Y. Wang, S. Hou, Superlatt. Microstruct. **83**, 422–430 (2015)

70. K. Karthik, S. Dhanuskodi, S. Prabukumar, C. Gobinath, S. Sivaramakrishnan, J. Mater. Sci. **29**, 5459–5471 (2018)

71. K. Milenova, I. Stambolova, V. Blaskov, A. Eliyas, S. Vassilev, M. Shipochka, J. Chem. Technol. Metal. **48**, 259–264 (2013)

72. M. Rezapour, N. Talebian, Mater. Chem. Phys. **129**, 249–255 (2011)

73. C. Rajendra, Pawar, Caroline Sunyong Lee. Appl. Catal. B **144**, 57–65 (2014)

74. P.K. Stoimenov, R.L. Klinger, G.L. Marchin, K.J. Klabunde, Langmuir **18**, 6679–6686 (2002)

75. L. Zhang, Y. Jiang, Y. Ding, M. Povey, D. York, Nanopart. Res. **9**, 479–489 (2007)

76. T.K. Rahul, N. Sandhyarani, Nanoscale **7**, 18259–18270 (2015)

77. R. Fagan, D.E. McCormack, D.D. Dionysiou, S.C. Pillai, Mater. Semicond. Process. **42**, 2–14 (2015)

78. M. Pelaez, N.T. Nolan, S.C. Pillai, M.K. Seery, P. Falaras, A.G. Kontos, P.S.M. Dunlop, J.W.J. Hamilton, J. Byrne, K. Oshea, M.H. Entezari, D.D. Dionysiou, Appl. Catal. B **125**, 331–349 (2012)

79. N. Padmavathy, R. Vijayaraghavan, Sci. Technol. Adv. Mater. **9**, 1–7 (2008)

80. Z.M. Xiu, Q.B. Zhang, H.L. Puppala, V.L. Colvin, P.J.J. Alvarez, Nano Lett. **12**, 4271–4275 (2012)

81. R. Menaka, R. Subiya, Int. J. Sci. Res. **5**, 269–271 (2016)

82. M. Vanaja, G. Gnanajobitha, K. Paulkumar, S. Rajeshkumar, C. Malarkodi, G. Annadurai, J. Nanostruct Chem. **3**, 3–17 (2013)